

# Commissioning, characterization and first high dose rate irradiations at a compact X-ray tube for microbeam and minibeam radiation therapy

Christian Petrich<sup>1,2,3,4,\*</sup>, Johanna Winter<sup>1,3,4,\*</sup>, Anton Dimroth<sup>1,3,5,\*</sup>, Thomas Beiser<sup>6,7</sup>,  
Monika Dehn<sup>1,6,7</sup>, Jessica Stolz<sup>1,4</sup>, Jacopo Frignani<sup>8</sup>, Stephanie E. Combs<sup>1,4</sup>, Franz  
Schilling<sup>8,9,10</sup>, Ghaleb Natour<sup>5,11</sup>, Kurt Aulenbacher<sup>6,7,12</sup>, Thomas E. Schmid<sup>1,4</sup>, Jan J.  
Wilkens<sup>1,2</sup>, and Stefan Bartzsch<sup>1,3,4</sup>

<sup>1</sup>Technical University of Munich, TUM School of Medicine and Health, Department of Radiation Oncology, TUM University Hospital, Munich, Germany

<sup>2</sup>Technical University of Munich, School of Natural Sciences, Department of Physics, Garching, Germany

<sup>3</sup>Heinz Maier-Leibnitz Zentrum (MLZ), Garching, Germany

<sup>4</sup>Helmholtz Zentrum München GmbH, German Research Center for Environmental Health, Institute of Radiation Medicine, Neuherberg, Germany

<sup>5</sup>Forschungszentrum Jülich GmbH, Institute of Technology and Engineering (ITE), Jülich, Germany

<sup>6</sup>Helmholtz-Institute Mainz, Accelerator Design and Integrated Detectors, Mainz, Germany

<sup>7</sup>GSI Helmholtzzentrum für Schwerionenforschung GmbH, Darmstadt, Germany

<sup>8</sup>Technical University of Munich, TUM School of Medicine and Health, Department of Nuclear Medicine, TUM University Hospital, Munich, Germany

<sup>9</sup>Technical University of Munich, Munich Institute of Biomedical Engineering, Garching, Germany

<sup>10</sup>German Cancer Consortium (DKTK), Partner Site Munich and German Cancer Research Center (DKFZ), Heidelberg, Germany

<sup>11</sup>ISF, Faculty of Mechanical Engineering, RWTH Aachen University, Aachen, Germany

<sup>12</sup>Johannes Gutenberg University, Institute for Nuclear Physics, Mainz, Germany

\* Shared first authorship.

## Abstract

**Background:** Minibeam and microbeam radiation therapy promise improved treatment outcomes through reduced normal tissue toxicity at better tumor control rates. The lack of suitable compact radiation sources limits the clinical application of minibeam to superficial tumors and renders it impossible for microbeams. We developed and constructed the first prototype of a compact line-focus X-ray tube (LFXT) with technology potentially suitable for clinical translation of minibeam and microbeams.

**Methods:** We give an overview of the commissioning process preceding the first operation, present optical and radiological focal spot characterization methods, and dosimetric measurements. Additionally, we report on first

preclinical *in vitro* cell and *in vivo* mouse brain irradiations conducted with the LFXT prototype.

**Results:** The focal spot characterization resulted in a strongly eccentric electron distribution with a width of 72.3  $\mu\text{m}$ . Dosimetry showed sharp microbeam dose profiles with steep lateral penumbras and a peak-to-valley dose ratio above 10 throughout a 70 mm thick PMMA phantom. An open-field dose rate of 4.3 Gy/s was measured at an acceleration voltage of 150 kV and a beam current of 17.4 mA at 150 mm distance from the focal spot. *In vitro* and *in vivo* experiments demonstrated the feasibility of the LFXT for minibeam and microbeam applications with field sizes of 1.5–2 cm. The mice displayed no observable side effects throughout the follow-up period after whole-brain 260  $\mu\text{m}$ -minibeam irradiation.

**Conclusion:** We successfully constructed and commissioned the first proof-of-concept LFXT prototype. Dosimetric characterizations of the achieved microbeam field showed the superiority of the LFXT compared to conventional X-ray tubes in terms of beam quality. In future developments, the remaining limitations of the prototype will be addressed, paving the way for improved minibeam and first ever microbeam radiation therapy in a clinical setting.

## 1 Introduction

Spatially fractionated radiation therapy (SFRT) is gaining recognition as a promising technique in cancer treatment by breaking with one of the central paradigms of conventional radiation therapy: Instead of delivering a homogeneous dose distribution to the target volume, the radiation field in SFRT is intentionally modulated into low-dose regions ("valleys") and regions receiving unconventionally high doses ("peaks"). Clinically applied SFRT methods include photon and proton grid and lattice radiation therapy. Several hundred patients with bulky, advanced tumors have been treated with such a dose modulation in the centimeter range [1–3].

Preclinical studies indicate that finer dose modulation results in a wider therapeutic window, leading to enhanced tumor control and at the same time reduced side effects such as radiation-induced toxicity [4, 5]. Thereby, minibeam and microbeam exhibit dose modulations in the millimeter and sub-millimeter / micrometer range, respectively. The wider therapeutic window of microbeams and minibeam compared to a conventional homogeneous dose distribution is attributed to various mechanisms, including anti-tumor immune activation, vascular effects, and bystander responses [6–8]. Preclinically, microbeam radiation therapy was shown to be highly effective in the treatment of radiation resistance tumors, such as brain, breast, and skin tumors, while minimizing side effects, *e.g.*, in the brain, thorax or abdomen [9–11]. Recently, Grams et al. [12] reported first clinical minibeam irradiations of skin tumors using a conventional orthovoltage X-ray tube and a custom-made minibeam collimator fixed to the patient. Patient outcomes indicated symptom relief

and positive tumor response. Current limitations of this clinical minibeam radiation therapy approach include very long irradiation times due to low dose rates and the restriction to superficial tumors, mainly due to a smearing of the minibeam pattern with increasing depth in tissue.

A widespread clinical implementation of minibeam and, especially, microbeam radiation therapy is challenging and requires considerable development in compact radiation sources, treatment planning, dosimetry, patient alignment, and standards of dose prescription and quality assurance. The major obstacle remains generating X-ray minibeam and microbeams that retain their sharp dose modulation at several centimeters of tissue depth, without relying on large, non-scalable third-generation synchrotrons such as the European Synchrotron (ESRF) in Grenoble, France, and the Australian Synchrotron in Melbourne, where most preclinical microbeam studies have been performed [13]. Achieving sharp microbeam dose patterns in patients requires orthovoltage, high dose-rate X-rays emitted from a source with a width comparable to the intended peak width. These characteristics mitigate adverse effects of secondary electron range, geometric blurring, and organ motion. Several compact radiation sources have been proposed for microbeam radiotherapy, including inverse Compton scattering sources [14, 15], carbon nanotube-based X-ray tubes [16, 17], and conventional X-ray tubes [18, 19]. However, these technologies have not reached the necessary dose rates and/or photon energies for a widespread clinical application of microbeam or minibeam radiation therapy.

Based on the line-focus X-ray tube (LFXT) concept, we developed and built the first compact X-ray microbeam and minibeam irradiator with technology suitable for clinical application [20–22]. Here, we report on the commissioning, microbeam dosimetry, and first preclinical minibeam and microbeam irradiations with our proof-of-concept LFXT prototype.

## 2 Methods

### 2.1 Commissioning of the line-focus X-ray tube prototype

The concept and technology development of the LFXT was described in previous publications [20–24]. In brief, our proof-of-concept LFXT prototype resembles conventional X-ray tubes with specific characteristics regarding the electron acceleration and focusing, the target rotation, and the photon beam extraction, as presented in figure 1. Electrons are emitted from a thermionic cathode, regulated by a control electrode, and accelerated towards a slotted anode by an applied voltage of up to 300 kV [22]. The beam pipe is surrounded by two quadrupole focusing magnets and a pair of dipole steering magnets at distances of 150 mm, 350 mm, and 250 mm to the cathode, respectively. The electron beam impinges perpendicularly onto the front surface of the target at a distance of 488 mm from the cathode, producing a focal spot with full widths at half maximum (FWHM) of  $0.05\text{ mm}\times 22\text{ mm}$  according to simulations [22]. The target (Plansee SE, Reutte, Austria) with a diameter of 240 mm incorporates a tungsten-rhenium conversion layer and rotates at frequencies of up to 200 Hz [23]. X-rays are extracted at an angle of  $45^\circ$  to the electron beam through a primary beam exit window at a distance of 110 mm and at an angle of nearly  $90^\circ$  through a secondary beam exit at a distance of 160 mm from the focal spot.

Behind the primary beam exit window, varying multislit collimators, apertures, and filters can be placed at a distance of 135 mm from the focal spot, shaping the X-ray beam into minibeam and microbeam fields. The collimator design accounts for the specific geometry and orientation of the focal spot in relation to the collimator, as presented in [24]. Three different collimators were produced with  $40\text{ }\mu\text{m}$ ,  $50\text{ }\mu\text{m}$ , and  $200\text{ }\mu\text{m}$ -wide slits with center-to-center distances of  $320\text{ }\mu\text{m}$ ,  $400\text{ }\mu\text{m}$ , and  $800\text{ }\mu\text{m}$ , respectively. The collimators have a square field size of 20 mm. A specialized holder allows for precise rotational and translational alignment with the focal spot.

To commission the LFXT prototype, the vacuum chamber was initially baked out to reduce residual

gases. The electron accelerator was then high-voltage conditioned with a cold cathode to withstand high acceleration voltages without insulation breakdowns. This involved intentionally inducing microscopic vacuum discharges around surface impurities, where locally enhanced electric field gradients caused their abrasion. Inserted for conditioning, four high-voltage resistors between the accelerator and the high-voltage power supply limited the current to protect sensitive components from occasional strong discharges. The time-intensive conditioning process was automated using an in-house protocol that adjusted the voltage in response to vacuum levels in the accelerator chamber. For cathode conditioning, the heating current was gradually increased until the temperature reached  $1130^\circ\text{C}$ . Subsequently, the high voltage was ramped up while the control electrode retained a potential of  $-500\text{ V}$  relative to the cathode to prevent uncontrolled electron acceleration. Carefully reducing this potential difference initiated electron acceleration through the anode onto the target, generating first X-rays.

### 2.2 Measurement of the focal spot

We employed optical imaging and radiographic pinhole and edge measurements to monitor and characterize the focal spot of the LFXT prototype. The X-ray source was operated during the first beam with an acceleration voltage of 150 kV and an electron beam current in the range of 1–6 mA.

*Optical measurement:* High-energy electrons of a few 100 keV emit transition radiation in the optical range when passing through material boundaries [25]. We installed a Raspberry Pi camera to capture this transition radiation from the focal spot. The viewport was oriented at a viewing angle of  $67^\circ$  towards the target surface, with the result that the focal spot shape appeared distorted.

*Pinhole measurements:* The pinhole was made from a 1 mm-thick tungsten plate with a  $25\text{ }\mu\text{m}$  diameter hole and centered between the focal spot and a CMOS X-ray detector (S15683-13, Hamamatsu Photonics K.K., Japan). The detector was positioned at a distance of 500 mm from the focal spot and had a nominal pixel pitch of  $20\text{ }\mu\text{m}$ . The geometric magnification was 1 along the short axis of the focal

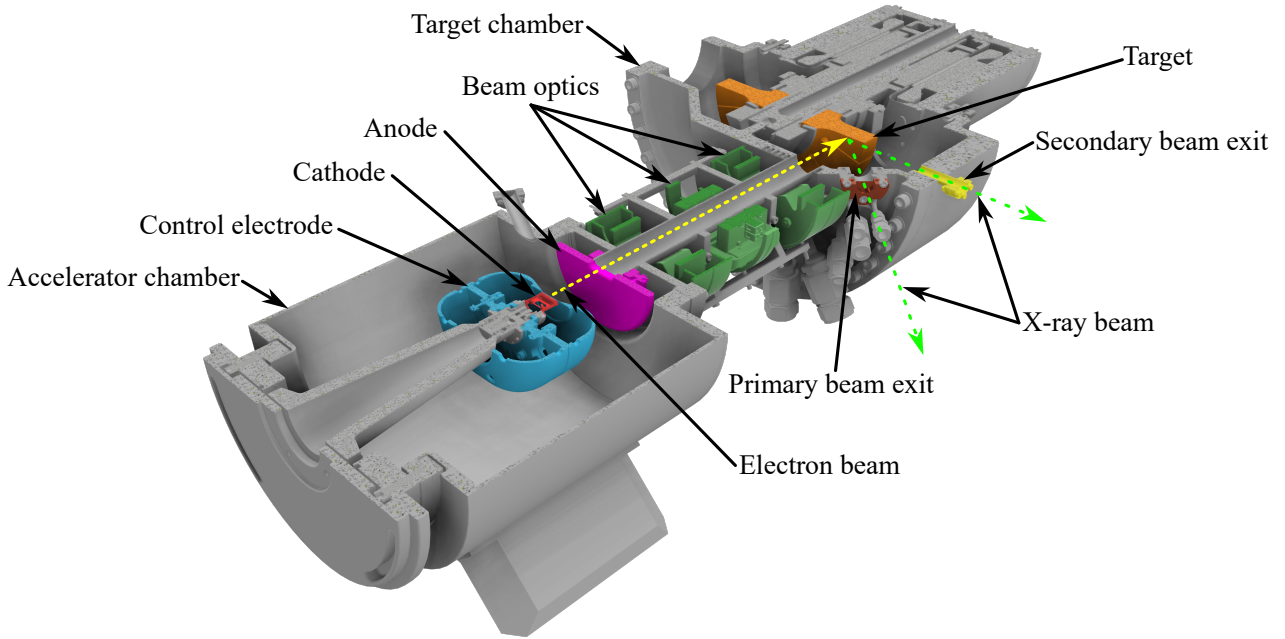


Figure 1: Horizontal section view through the vacuum chamber of the LFXT prototype. The accelerator and target chambers are connected by the electron beam pipe.

spot and  $1/\sqrt{2}$  along the long axis of the focal spot due to the  $45^\circ$  angle between the central beam axis and the target surface normal. Flat- and dark-field image corrections were applied as explained by Petrich et al. [24].

*Edge measurements:* A 2 mm-thick tungsten plate with a sharp edge was centered between the focal spot and the CMOS detector. The edge was initially aligned approximately parallel to the long axis of the focal spot to measure the line-spread function (LSF) along the short axis. To optimize rotational alignment, the tungsten edge was rotated around the beam axis in  $1^\circ$  steps. Images of each edge position were flat- and dark-field corrected and processed as described by Petrich et al. [24], resulting in individual LSFs. The optimal alignment corresponded to the LSF with the smallest FWHM.

### 2.3 Dosimetry

After optimizing the electron beam focusing optics, the dose was measured as open-field dose rate, and microbeam and minibeam dose distributions were evaluated within a PMMA phantom and for preclinical experiments.

The open-field dose rate was measured in air at a distance of 131 mm from the focal spot.

A microDiamond detector was used for dosimetry with a Unidos electrometer (both PTW Freiburg GmbH, Freiburg, Germany) after cross-calibration using a Farmer-type ionization chamber (TM30010, PTW Freiburg GmbH) at a conventional X-ray tube (RS225, Xstrahl, Suwanee, GA, USA) with similar beam quality. Dose rate linearity with respect to beam current was assessed using the microDiamond detector without additional filtering. Acceleration voltages of 135 kV and 150 kV were applied, while the voltage of the control electrode was gradually reduced, leading to an electron beam current of up to 17.4 mA.

Microbeam and minibeam dose distributions were measured using radiochromic films (Gafchromic EBT3 films, Ashland, Wilmington, DE, USA). Film calibration was performed in the range of 0–10 Gy as described previously [18, 26]. Peak and valley doses were defined as the means within the central 60% of the peak and valley regions, with valleys being the regions between peaks defined by their FWHMs. Peak-to-valley dose ratios (PVDRs) were calculated by dividing the average peak dose by the average valley dose.

The PVDR of a microbeam radiation field was evaluated using the collimator with a  $50\ \mu\text{m}$  slit width and a  $400\ \mu\text{m}$  center-to-center distance.

Measurements were performed in a phantom composed of 14 PMMA plates, each with a thickness of 5 mm and a size of 40 mm  $\times$  40 mm, with radiochromic films inserted between the plates. The phantom surface was placed at a distance of 29 mm from the collimator, *i.e.*, 163 mm from the focal spot. An aperture limited the field size to 20 mm  $\times$  20 mm at the phantom surface. A 150 kVp spectrum was used with a filtering of 1 mm aluminum, and the electron beam current was set to 6 mA.

For comparison, a similar measurement was performed at a small-animal irradiator (XenX, Xstrahl) that was in-house transformed into a microbeam irradiation device using the broad focal spot (3.55 mm  $\times$  2.95 mm), a 225 kVp spectrum, and a filtering of 1 mm aluminum [18, 27]. The field size, slit width and distance matched those of the LFXT setup, while the phantom was placed back-to-back to the collimator at a distance of 212 mm from the focal spot.

## 2.4 First *in vitro* and *in vivo* experiments

To assess the feasibility of preclinical irradiations at the LFXT prototype, cancer cells were irradiated with microbeams *in vitro*. Additionally, glioblastoma-bearing mice were irradiated with minibeam *in vivo* as part of a preclinical study, of which we present one representative case as proof of concept.

In the *in vitro* proof-of-concept experiment, established human-derived epithelial non-small cell lung carcinoma cells (A549, ATCC, Manassas, USA) were irradiated at a distance of 150 mm from the focal spot using a 25 mm  $\times$  25 mm microbeam field. The collimator had a slit width of 50  $\mu$ m and a slit center-to-center distance of 400  $\mu$ m. At an acceleration voltage of 135 kV and an electron beam current of 8 mA, the peak dose amounted to 10 Gy with a peak dose rate of 13 Gy/min, as measured with radiochromic films. Following irradiation, the cells were stained with  $\gamma$ -H2AX (Merck KGaA, Darmstadt, Germany) for DNA double-strand breaks, counterstained with Hoechst 33342 (Thermo Fisher Scientific, Waltham, USA), and scanned using an inverted microscope (Axio Observer 7, Carl Zeiss

Microscopy GmbH, Jena, Germany).

The animal experiment was authorized by the local government authorities (Regierung von Oberbayern, Munich, Germany; license 55.2.2532.Vet-02-20-39) and conducted in compliance with German animal welfare regulations. Six-week-old female C57Bl6/N mice (Charles River Laboratories GmbH, Sulzfeld, Germany) were anesthetized, and 50 000 GL261 murine glioblastoma multiforme cells (Leibniz Institute DSMZ GmbH, Braunschweig, Germany), were stereotactically inoculated into the right caudate nucleus. Tumor growth was monitored twice per week by T1-weighted MRI using gadolinium-Dota contrast agent (DotaVision, röntgen bender GmbH & Co. KG, Baden-Baden, Germany). When tumors reached a volume of 15 mm<sup>3</sup>, total brain minibeam irradiation was performed.

For irradiation, the anesthetized mouse was placed on a 3D-printed bed designed for brain irradiations with the LFXT prototype and mounted on a six-axis robotic arm (MECA500, Mecademic, Montreal, Canada) for precise positioning. Alignment was verified using a birds-eye camera, a beam's-eye camera (via a mirror), and a custom Python program displaying the radiation field on a fluorescent screen image. The minibeam collimator with 200  $\mu$ m-wide slits spaced 800  $\mu$ m apart was used with a squared aperture of 10 mm edge length. The isocenter was defined at the center of the brain and mouse bed, located 55 mm behind the multislit collimator and 191.5 mm from the focal spot. Film dosimetry at the isocenter showed a peak width of (260  $\pm$  4)  $\mu$ m, a center-to-center distance of (1119  $\pm$  3)  $\mu$ m, and a field size of 15 mm  $\times$  15 mm. The dose rate in the peaks amounted to 4.8 Gy/min using a 150 kVp spectrum with 0.5 mm aluminum filtering. This minibeam field behind the primary beam exit window was combined with a broad-beam field behind the secondary X-ray exit window to achieve a PVDR of 10. Thereby, the total peak dose amounted to 150 Gy and the valley dose to 15 Gy at a depth of 5 mm, *i.e.*, at the center of the brain. The isocenter for the broad-beam irradiation was located 266 mm from the focal spot. The electron beam current was held at 6 mA, yielding a dose rate of 4.8 Gy/min in the peak and 0.2 Gy/min in the valley behind the primary

beam exit window and 0.6 Gy/min for the broad beam behind the secondary beam exit window. The mouse was followed up post-treatment with repeated T1-weighted MRI using a RARE sequence on a 7T preclinical scanner (Discovery MR901, Agilent, Santa Clara, CA, USA; Avance III HD electronics, Bruker BioSpin MRI GmbH, Ettlingen, Germany) with a mouse brain 1H surface coil (RAPID Biomedical GmbH, Rimpar, Germany).

### 3 Results

#### 3.1 Commissioning

After bake-out and cooling down, vacuum pressures of  $3.9 \times 10^{-9}$  mbar and  $2.5 \times 10^{-8}$  mbar were achieved in the accelerator chamber and target chamber of the LFXT prototype, respectively. Figure 2 shows the vacuum pressure in the accelerator chamber and the corresponding acceleration voltage during high-voltage conditioning of the electron accelerator. The vacuum pressure showed high-frequency pressure spiking, attributed to minor discharges that effectively evaporated surface impurities. The voltage gradient was adapted by improvements to the automatic conditioning protocol. The conditioning was performed up to 180 kV before conducting experiments at 150 kV.

With the cathode heated and high voltage applied, an X-ray beam was produced by decreasing the potential difference between the control electrode and the cathode. Radiographic images of both open and microbeam fields were then acquired with the CMOS X-ray detector.

#### 3.2 Measurement of the focal spot

The adjustments of the electron optics were performed stepwise based on the focal spot visualization. Initially, the optical method was used for qualitative visualization while adjusting only the quadrupole magnets. Once preliminary focusing parameters were established, the pinhole and edge methods were applied to quantitatively characterize the achieved focal spot. Figure 3 presents the results of the three characterization methods. In both the optical image and the radiological image acquired using the 25  $\mu\text{m}$  pinhole, the focal spot exhibits

the desired strongly eccentric shape, with a length of approximately 6 mm. From both radiological methods, the focal spot width was derived by fitting a Gaussian function, resulting in a width of  $(144.3 \pm 0.8) \mu\text{m}$  FWHM from the pinhole method and a width of  $(72.3 \pm 0.3) \mu\text{m}$  FWHM from the edge method. The difference in measured focal spot width can be explained by the inherent broadening effect of the pinhole on the acquired focal spot projection.

#### 3.3 Dosimetry

With optimized electron beam focusing, open-field dose rates at the primary beam exit window were obtained from single measurements. The maximum tested electron beam current of 17.4 mA at an acceleration voltage of 150 kV yielded a dose rate of 4.3 Gy/s. A beam current of 12.0 mA at an acceleration voltage of 135 kV yielded a dose rate of 2.5 Gy/s. Both measurements were performed at 150 mm from the focal spot. Measurements at lower electron beam currents confirmed a linear relationship between dose rate and beam current, with a steeper slope at the higher acceleration voltage.

Radiochromic film dosimetry showed sharp microbeam dose profiles with steep lateral penumbras throughout the PMMA phantom using the LFXT prototype. Lateral peak penumbras (80% to 20% of the peak-to-valley dose difference) were 27  $\mu\text{m}$  at the phantom surface and 41  $\mu\text{m}$  at a depth of 71 mm. The peak dose rate was  $(3.3 \pm 0.2)$  Gy/min at the phantom surface,  $(2.7 \pm 0.1)$  Gy/min at 5 mm, and  $(2.0 \pm 0.1)$  Gy/min at 10 mm depth with an electron beam current of 6 mA, an acceleration voltage of 150 kV, a collimator slit width of 50  $\mu\text{m}$ , and a center-to-center spacing of 400  $\mu\text{m}$ . The uncertainties mainly resulted from film dosimetry derived from Bartzsch et al. [26].

Figure 4 demonstrates considerably sharper dose profiles and higher peak doses with the LFXT prototype compared to the profiles measured at the conventional small-animal irradiator XenX, both obtained at 22 mm depth in PMMA. It is essential to point out that, at the LFXT, the PMMA phantom had a distance of 29 mm from the multislit collimator, whereas the phantom was in direct contact with the multislit collimator at the XenX.

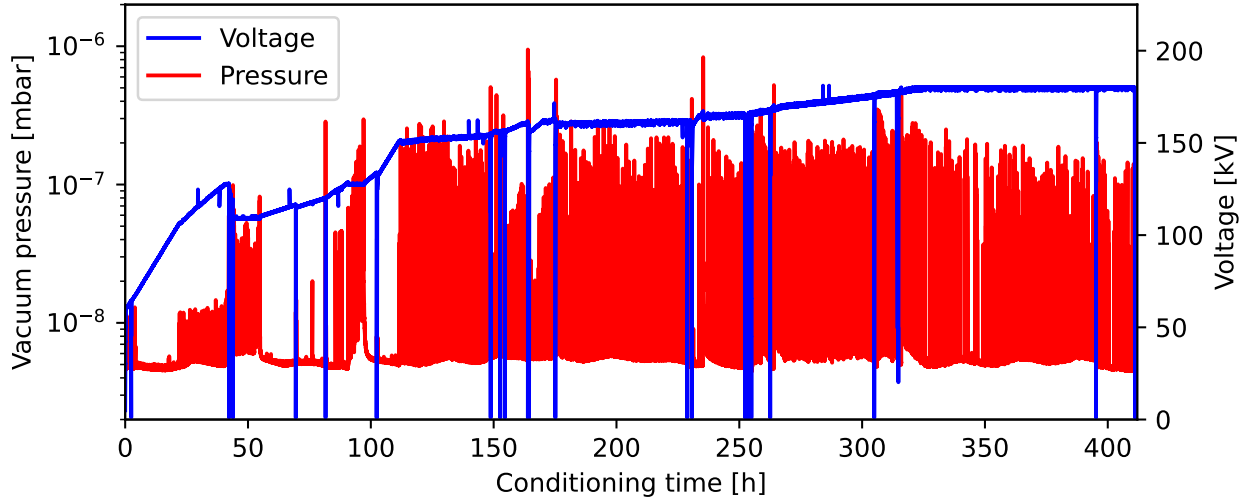


Figure 2: Vacuum pressure and applied voltage during high-voltage conditioning. The red line depicts the vacuum pressure in the accelerator chamber, the blue line depicts the acceleration voltage between cathode and anode. The conditioning time reflects active phases only. Adapted from [28].

At the LFXT, the PVDR decreased with depth from 25.4 at the phantom surface to 17.0 at 5 mm and 13.4 at 10 mm depth, while it approached approximately 10 from a depth of 30 mm until the end of the phantom. Published measurement data from the biomedical beamline ID17 at the European Synchrotron Radiation Facility (ESRF) with the same field size of  $20\text{ mm} \times 20\text{ mm}$  and the preclinical spectrum (mean energy of 105 keV [29]) was used for additional comparison [26]. The ESRF produced markedly higher PVDRs than the LFXT, mainly due to a smaller X-ray emitter and higher mean energy. The measurements at the XenX showed comparable PVDRs as at the LFXT up to 5 mm depth. For larger depths, the PVDR of the XenX decreased considerably faster than that of the LFXT and approached 1 due to a larger focal spot size and the resulting geometric blurring of the microbeam dose profile. Relative standard deviations of the mean PVDRs remained below 2% across all depths.

### 3.4 First preclinical experiments

Figure 5a shows a fluorescence microscopy image of human non-small cell lung carcinoma cells, illustrating spatially resolved DNA double-strand breaks 30 min post-irradiation. The microbeam irradiation effects are distinctly observable with

high-dose regions (peaks) exhibiting pronounced  $\gamma$ -H2AX foci accumulation, indicating considerable DNA damage. Conversely, the low-dose regions (valleys) show substantially fewer foci, corresponding to reduced DNA damage. This differential response underscores the capability of the LFXT to deliver precise microbeam fields.

Figure 5b shows the setup used for mouse irradiations at the LFXT prototype. Figure 5c presents a T1-weighted MR image of an irradiated mouse brain, with the entrance direction of the minibeam field indicated by arrows. The peak regions of the minibeam field are distinctly visible as bright stripes following contrast agent injection of gadolinium-DOTA. These elevated signal intensities in the minibeam channels after contrast-enhanced T1-weighted MRI are presumably attributed to increased vascular permeability. Throughout the follow-up period of up to 53 days, tumor response was observed, and the mouse showed no side effects or neurological dysfunctions attributable to the minibeam irradiations, despite peak doses of 150 Gy.

## 4 Discussion

We demonstrated the implementation of the LFXT as a compact radiation source for microbeam and minibeam radiation therapy. At the LFXT prototype,

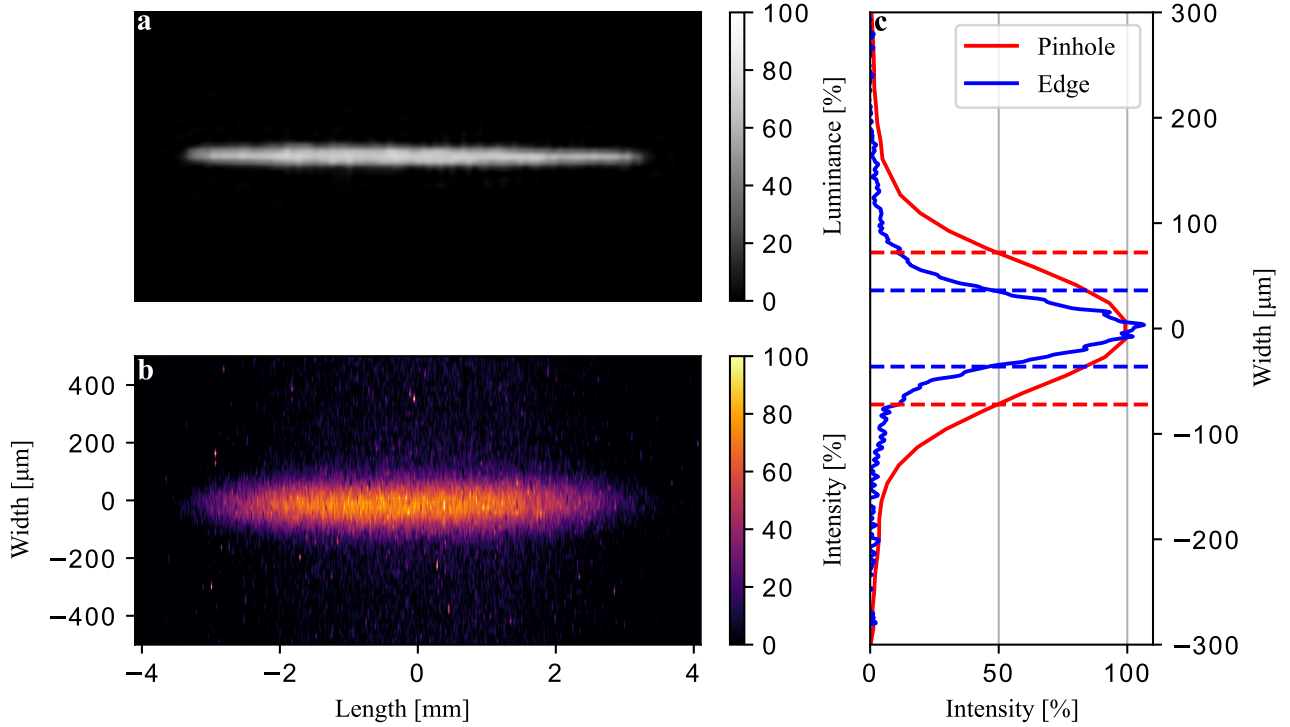


Figure 3: Results of focal spot characterizations using optical and radiological methods. **a** Normalized luminance of the focal spot visualized with a conventional optical camera. Due to distortions induced by the viewing angle, no absolute dimensions are given. **b** Radiological intensity distribution in two dimensions (with different scaling) measured using a 25  $\mu\text{m}$ -diameter pinhole. **c** Vertical line-spread functions (LSFs) obtained from the radiological pinhole and edge methods. The LSF resulting from the pinhole measurement exhibits a FWHM of  $(144.3 \pm 0.8) \mu\text{m}$ , while the LSF resulting from the edge measurement exhibits a FWHM of  $(72.3 \pm 0.3) \mu\text{m}$ , shown as dashed lines. Adapted from [28].

the microbeam PVDR remained above 10 throughout a 70 mm-thick phantom for an entry field size of  $20 \times 20 \text{ mm}^2$ . In contrast, the PVDR values dropped below 3 at a depth of 25–54 mm for field sizes of 3–10 cm for the first clinical minibeam irradiations [12], and at a depth of 31 mm for own measurements at a conventional X-ray tube, consistent with previously published data [18]. This rapid decrease in PVDR at conventional X-ray tubes, resulting from their large focal spot size, restricts their application in microbeam and minibeam radiation therapy to superficial tumors. Furthermore, the geometric blurring caused by the large focal spot requires target volumes to be positioned in close proximity to the multislit collimator for conventional X-ray tubes. In contrast, the LFXT maintains sharp dose profiles at several centimeters distance from the collimator, enabling more flexible irradiation positions and treatment of deeper-seated targets. Microbeam experiments at the European Synchrotron

Radiation Facility showed higher PVDR values in depth, similar to measurements at the Australian Synchrotron [30]. The higher PVDR values for the synchrotron experiments resulted mainly from a smaller effective radiation source size (52  $\mu\text{m}$  FWHM [31] and 38  $\mu\text{m}$  FWHM [32]) and higher mean energies of 105 keV [29] and 61 keV [33] for the ESRF and the Australian Synchrotron, respectively, compared to 53 keV at the LFXT, obtained by own Monte Carlo simulations. Even though synchrotrons provide attractive parameters for preclinical microbeam experiments, they are ineligible for clinical application due to their enormous infrastructural and financial requirements. The asymptotic behavior of the PVDR at the LFXT can be explained by two factors, considering a source size smaller than the collimator slit width. First, geometric magnification affects the peak penumbra and the center-to-center distance equally. Second, photon scattering from peaks into valleys reaches an equilibrium beyond a depth

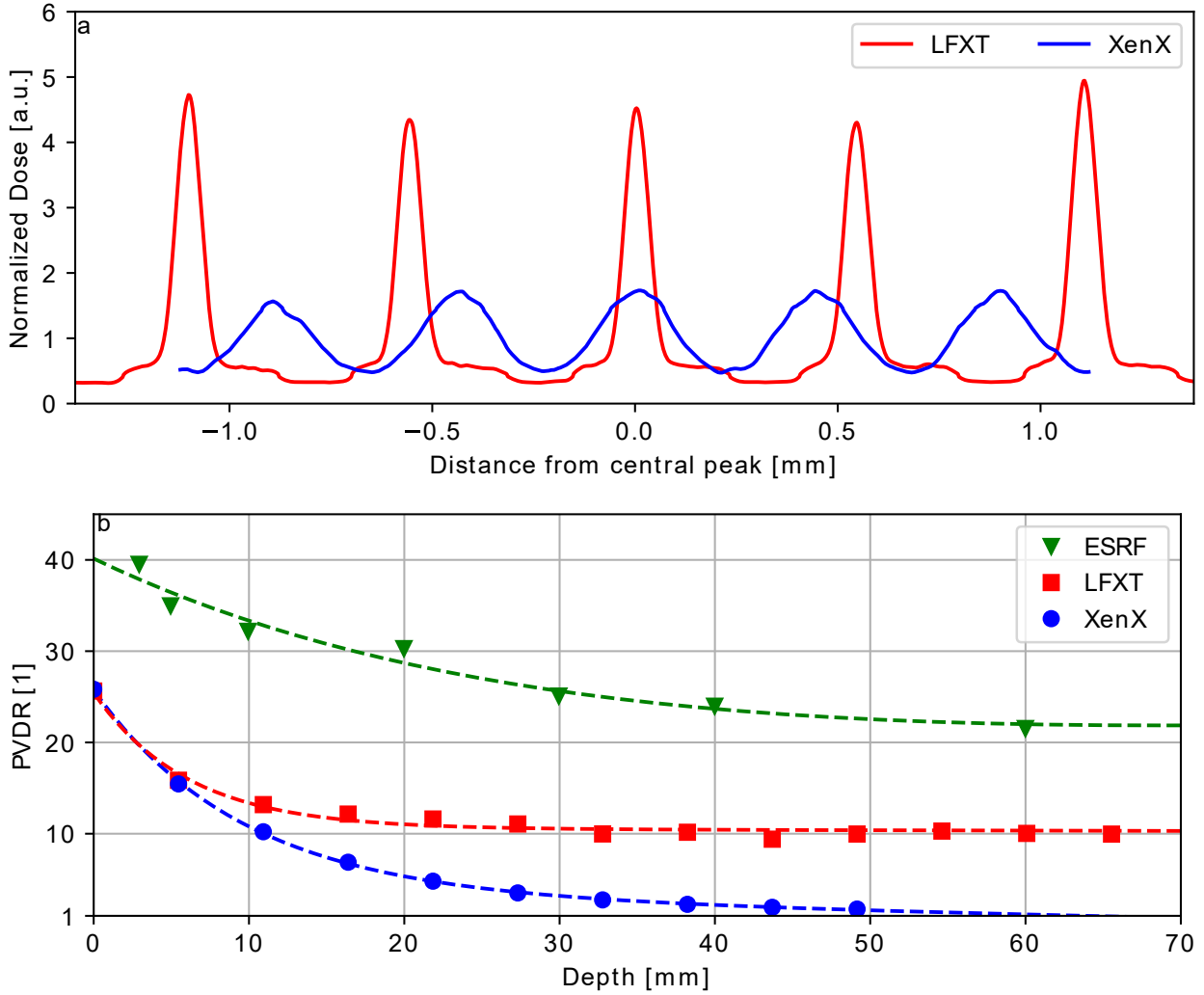


Figure 4: Comparison of microbeam dosimetry at different X-ray sources. **a** The central five peaks of the microbeam dose profiles at a depth of 22mm measured at the line-focus X-ray tube (LFXT) and a conventional small-animal irradiator (XenX). The profiles are normalized such that their mean values equal 1. **b** Measured peak-to-valley dose ratio (PVDR) in PMMA at the LFXT, the European Synchrotron Radiation Facility (ESRF) [26], and the XenX. Dashed lines indicate the trend of the measurement points fitted to the function  $PVDR = \exp(a \cdot x + b) + c \cdot x + d$ , where  $x$  is the depth. The relative standard errors of the mean were below 2% for the LFXT and XenX measurements and are not shown for clarity. Adapted from [28].

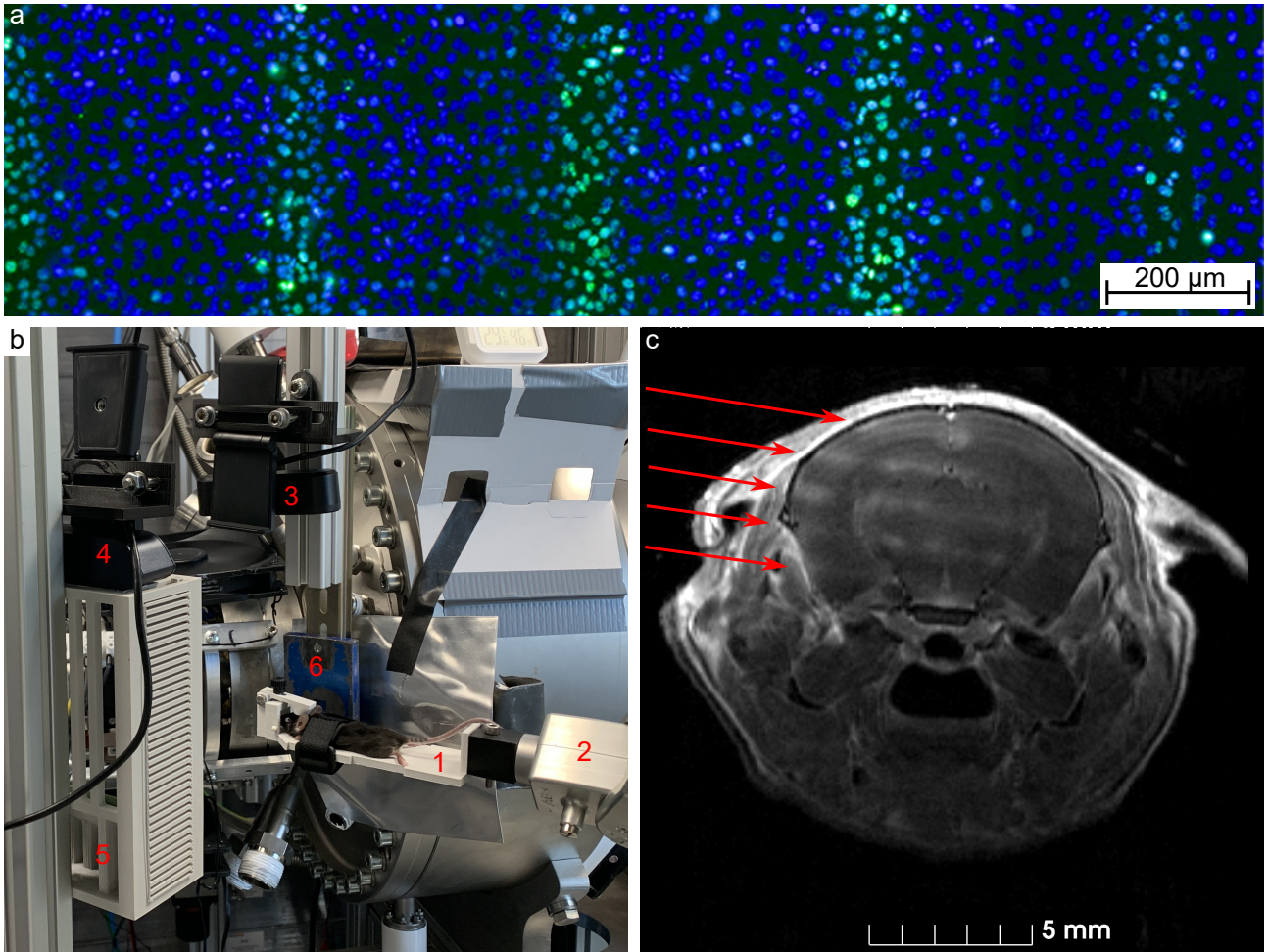


Figure 5: **a** Cells irradiated with microbeams stained against  $\gamma$ -H2AX (green) and counterstained with Hoechst (blue). **b** Positioning of a mouse for the irradiation of an orthotopic brain tumor with the mouse bed (1), the robot (2), a birds-eye camera (3), a beams-eye camera (4) with a mirror (5), and collimators (6) in front of the primary beam exit window. **c** T1-weighted MRI scan of a mouse brain 21 days post irradiation with minibeam stripes visible as bright stripes.

determined by the photon energy. The PVDR achieved at synchrotrons is expected to show the same behavior, but at larger depths due to the higher mean photon energy.

Our study estimates that, at the design parameters of 300 kV and 300 mA, the LFXT can achieve peak dose rates of 12 Gy/s at 5 mm depth for a setup comparable to the minibeam mouse irradiations, *i.e.*, at a distance of 200 mm from the focal spot. This estimate is extrapolated from the peak dose rate of 4.8 Gy/min during the mouse irradiation (6 mA, 150 kV, filtering of 0.5 mm aluminum), accounting for a factor 3 difference in dose rate efficiency between 300 kV and 150 kV [34]. This estimate is comparable to the previously simulated dose rate of 12 Gy/s in a broad beam field at a depth of 2 mm at 200 mm

from the focal spot with a 1 mm aluminum filter in the 300 kVp spectrum [35]. In comparison, the first clinical minibeam irradiations were delivered below 0.12 Gy/min peak dose rate at 1 cm depth [12].

The measured focal spot width of  $(72.3 \pm 0.3) \mu\text{m}$  FWHM was approximately 44% larger than the designed width of 50  $\mu\text{m}$ , while the measured focal spot length of 6 mm was substantially smaller than the intended 22 mm. This shorter focal spot length has no influence on the generated microbeam dose profiles and can be explained by the high potential difference between the control electrode and the cathode to limit the electron beam current, which cuts off the outer portions of the beam. The increased focal spot width can be attributed not only to the ongoing optimization of the electron optics but also to the

lower acceleration voltage of 150 kV compared to the designed voltage of 300 kV, which resulted in a larger geometrical beam emittance and consequently a broader focal spot [22]. As demonstrated, the currently achieved focal spot width is sufficient for generating microbeam and minibeam treatment fields for preclinical research. For operation at higher acceleration voltages and beam currents, the focal spot will be further optimized by putting the steerer magnet into operation.

The *in vitro* and *in vivo* experiments demonstrated the feasibility of the LFXT for preclinical minibeam and microbeam applications. The LFXT concept holds promise for clinical applications of both microbeam and minibeam radiation therapy. The expected increase in dose rate can substantially reduce exposure times, making such treatments more practical and efficient in clinical settings. In contrast to conventional X-ray tubes, the LFXT achieves high dose rates and sharp dose profiles at several centimeter tissue depth, which is essential for effective SFRT. Additionally, the control electrode enables triggering and thereby gating of the X-ray beam in a millisecond range, which improves precision, particularly for moving targets or adaptive treatment strategies. The small size and lower requirements for radiation shielding due to the lower photon energy compared to conventional linear accelerators allow a highly flexible integration into clinical environments.

While the LFXT was successfully commissioned and employed in first preclinical experiments, it remains at a prototype stage, with several challenges still limiting beam power. Future developments will focus on optimizing beam quality with a narrower focal spot and higher X-ray energy, increasing dose rate, and ensuring high reliability of the radiation source. Expanding preclinical studies, including exploiting synergies with immunotherapy, will help to better understand the biological mechanisms underlying microbeam and minibeam radiation therapy and thereby pave the way for clinical translation. The successful implementation of the LFXT into clinical practice could substantially advance cancer treatment by making microbeam and minibeam radiation therapy more accessible and widely applicable in oncology.

## 5 Conclusion

The first prototype of the LFXT was successfully set up and commissioned as proof of concept. Technical and biological experiments validated its suitability for preclinical microbeam and minibeam radiation therapy. As the LFXT concept is the only suitable compact radiation source that can generate sharp microbeam and minibeam dose distributions at several centimeter depth in tissue with high dose rates, the development and implementation of this LFXT prototype marks a considerable step towards a wide clinical application of microbeam and minibeam radiation therapy.

## Acknowledgments

This work was supported by the German Research Foundation (Deutsche Forschungsgemeinschaft) [grant number 459947066] and through the Emmy Noether Program [grant number 416790481], the German Federal Ministry of Education and Research (BMBF) through the program GO-Bio initial [grant number 16LW0396 and grant number 16LW0638K], and the Innovation Fund at Forschungszentrum Jülich.

## References

- [1] Wu X et al. “The Technical and Clinical Implementation of LATTICE Radiation Therapy (LRT)”. In: *Radiation Research* 194 (6 2020). DOI: 10.1667/RADE-20-00066.1.
- [2] Mayr NA et al. “Practice Patterns of Spatially Fractionated Radiation Therapy: A Clinical Practice Survey”. In: *Advances in Radiation Oncology* 9 (2 2024), p. 101308. DOI: 10.1016/j.adro.2023.101308.
- [3] Mohiuddin M et al. “Early clinical results of proton spatially fractionated GRID radiation therapy (SFGRT)”. In: *British Journal of Radiology* 93 (1107 2019), p. 20190572. DOI: 10.1259/bjr.20190572.
- [4] Subramanian N et al. “Superior Anti-Tumor Response After Microbeam and Minibeam Radiation Therapy in a Lung Cancer Mouse

- Model”. In: *Cancers* 17 (1 2025), p. 114. DOI: 10.3390/cancers17010114.
- [5] Griffin RJ et al. “Microbeam Radiation Therapy Alters Vascular Architecture and Tumor Oxygenation and is Enhanced by a Galectin-1 Targeted Anti-Angiogenic Peptide”. In: *Radiation Research* 177 (6 2012), pp. 804–812. DOI: 10.1667/RR2784.1.
- [6] Lukas L et al. “Immune Priming with Spatially Fractionated Radiation Therapy”. In: *Current Oncology Reports* 25 (12 2023), pp. 1483–1496. DOI: 10.1007/s11912-023-01473-7.
- [7] Song CW et al. “Preferential Tumor Vascular Damage Is the Common Antitumor Mechanism of High-Dose Hypofractionated Radiation Therapy: SABR, Spatially Fractionated Radiation Therapy, and FLASH Radiation Therapy”. In: *International Journal of Radiation Oncology\*Biophysics* 117 (3 2023), pp. 701–704. DOI: 10.1016/j.ijrobp.2023.05.015.
- [8] Jenkins SV et al. “Bystander Effects in Spatially Fractionated Radiation Therapy: From Molecule To Organism To Clinical Implications”. In: *Seminars in Radiation Oncology* 34 (3 2024), pp. 284–291. DOI: 10.1016/j.semradonc.2024.05.004.
- [9] Fernandez-Palomo C et al. “Animal Models in Microbeam Radiation Therapy: A Scoping Review”. In: *Cancers* 12 (3 2020), p. 527. DOI: 10.3390/cancers12030527.
- [10] Eling L et al. “Ultra high dose rate Synchrotron Microbeam Radiation Therapy. Preclinical evidence in view of a clinical transfer”. In: *Radiotherapy and Oncology* 139 (2019), pp. 56–61. DOI: 10.1016/j.radonc.2019.06.030.
- [11] Smyth LML et al. “Comparative toxicity of synchrotron and conventional radiation therapy based on total and partial body irradiation in a murine model”. In: *Scientific reports* 8 (1 2018), pp. 1–11. DOI: 10.1038/s41598-018-30543-1.
- [12] Grams MP et al. “Minibeam Radiation Therapy Treatment (MBRT): Commissioning and First Clinical Implementation”. In: *International Journal of Radiation Oncology\*Biophysics* 120 (5 2024), pp. 1423–1434. DOI: 10.1016/j.ijrobp.2024.06.035.
- [13] Bartzsch S et al. “Technical advances in x-ray microbeam radiation therapy”. In: *Physics in Medicine & Biology* 65 (2 2020), 02TR01. DOI: 10.1088/1361-6560/ab5507.
- [14] Jacquet M and Suortti P. “Radiation therapy at compact Compton sources”. In: *Physica Medica* 31 (6 2015), pp. 596–600. DOI: 10.1016/j.ejmp.2015.02.010.
- [15] Dombrowsky AC et al. “A proof of principle experiment for microbeam radiation therapy at the Munich compact light source”. In: *Radiation and Environmental Biophysics* 59 (2020), pp. 111–120. DOI: 10.1007/s00411-019-00816-y.
- [16] Schreiber EC and Chang SX. “Monte Carlo simulation of a compact microbeam radiotherapy system based on carbon nanotube field emission technology”. In: *Medical Physics* 39 (8 2012), pp. 4669–4678. DOI: 10.1118/1.47282200.
- [17] Hadsell M et al. “Pilot study for compact microbeam radiation therapy using a carbon nanotube field emission micro-CT scanner”. In: *Medical Physics* 41 (6Part1 2014), p. 061710. DOI: 10.1118/1.4873683.
- [18] Ahmed M et al. “In Vivo Microbeam Radiation Therapy at a Conventional Small Animal Irradiator”. In: *Cancers* 16 (3 2024). DOI: 10.3390/cancers16030581.
- [19] Bartzsch S et al. “A preclinical microbeam facility with a conventional x-ray tube”. In: *Medical Physics* 43 (12 2016), pp. 6301–6308. DOI: 10.1118/1.4966032.
- [20] Bartzsch S and Oelfke U. “Line focus x-ray tubes—a new concept to produce high brilliance x-rays”. In: *Physics in Medicine & Biology* 62 (22 2017), p. 8600. DOI: 10.1088/1361-6560/aa910b.

- [21] Winter J et al. “Clinical microbeam radiation therapy with a compact source: specifications of the line-focus X-ray tube”. In: *Physics and Imaging in Radiation Oncology* 14 (2020), pp. 74–81. DOI: 10.1016/j.phro.2020.05.010.
- [22] Matejcek C et al. “A novel electron source for a compact x-ray tube for microbeam radiotherapy with very high dose rates”. In: *Physica Medica* 106 (2023), p. 102532. DOI: 10.1016/j.ejmp.2023.102532.
- [23] Winter J et al. “Heat management of a compact x-ray source for microbeam radiotherapy and FLASH treatments”. In: *Medical Physics* 49 (5 2022), pp. 3375–3388. DOI: 10.1002/mp.15611.
- [24] Petrich C et al. “The compact line-focus X-ray tube for microbeam radiation therapy — Focal spot characterisation and collimator design”. In: *Physica Medica* 129 (2025), p. 104861. DOI: 10.1016/j.ejmp.2024.104861.
- [25] Yamamoto N et al. “Light emission from surfaces, thin films and particles induced by high-energy electron beam”. In: *Surface and Interface Analysis* 31 (2 2001), pp. 79–86. DOI: 10.1002/sia.958.
- [26] Bartzsch S et al. “Micrometer-resolved film dosimetry using a microscope in microbeam radiation therapy”. In: *Medical Physics* 42 (7 2015), pp. 4069–4079. DOI: 10.1118/1.4922001.
- [27] Treibel F et al. “Establishment of Microbeam Radiation Therapy at a Small-Animal Irradiator”. In: *International Journal of Radiation Oncology\*Biophysics\*Physics* 109 (2 2021), pp. 626–636. DOI: 10.1016/j.ijrobp.2020.09.039.
- [28] Petrich C. “Development and commissioning of a novel compact X-ray source for preclinical microbeam radiotherapy”. en. PhD thesis. Technische Universität München, 2025. URL: <https://mediatum.ub.tum.de/1764823>.
- [29] Crosbie JC et al. “Energy spectra considerations for synchrotron radiotherapy trials on the ID17 bio-medical beamline at the European Synchrotron Radiation Facility”. In: *Journal of synchrotron radiation* 22 (4 2015), pp. 1035–1041. DOI: 10.1107/S1600577515008115.
- [30] Dipuglia A et al. “Validation of a Monte Carlo simulation for Microbeam Radiation Therapy on the Imaging and Medical Beamline at the Australian Synchrotron”. In: *Scientific Reports* 9 (1 2019), p. 17696. DOI: 10.1038/s41598-019-53991-9.
- [31] Mittone A et al. “Multiscale pink-beam microCT imaging at the ESRF-ID17 biomedical beamline”. In: *Journal of Synchrotron Radiation* 27 (5 2020), pp. 1347–1357. DOI: 10.1107/S160057752000911X.
- [32] Stevenson AW et al. “First experiments on the Australian Synchrotron Imaging and Medical beamline, including investigations of the effective source size in respect of X-ray imaging”. In: *Journal of Synchrotron Radiation* 17 (1 2010), pp. 75–80. DOI: 10.1107/S0909049509041788.
- [33] Crosbie JC et al. “Reference dosimetry at the Australian Synchrotron’s imaging and medical beamline using free-air ionization chamber measurements and theoretical predictions of air kerma rate and half value layer”. In: *Medical Physics* 40 (6Part1 2013). DOI: 10.1118/1.4803675.
- [34] Vogt HG and Schultz H. *Grundzüge des praktischen Strahlenschutzes*. 6th ed. Carl Hanser Verlag GmbH & Co. KG, 2011. DOI: 10.3139/9783446428935.
- [35] Winter J. “Microbeam radiotherapy on the path to clinical application: A powerful compact x-ray source and microbeam treatment planning”. en. PhD thesis. Technical University of Munich, 2023, p. 207. URL: <https://mediatum.ub.tum.de/1687953>.